The Journal of Experimental Biology 211, 2669-2677
Published by The Company of Biologists 2008
doi:10.1242/jeb.015883

The 'upstream wake' of swimming and flying animals and its correlation with propulsive efficiency

Jifeng Peng[1,*] and John O. Dabiri[1,2]

[1]Bioengineering, California Institute of Technology and [2]Graduate Aeronautical Laboratories, California Institute of Technology, Pasadena, CA 91125, USA

*Author for correspondence (jfpeng@caltech.edu)

Accepted 18 May 2008

SUMMARY

The interaction between swimming and flying animals and their fluid environments generates downstream wake structures such as vortices. In most studies, the upstream flow in front of the animal is neglected. In this study, we demonstrate the existence of upstream fluid structures even though the upstream flow is quiescent or possesses a uniform incoming velocity. Using a computational model, the flow generated by a swimmer (an oscillating flexible plate) is simulated and a new fluid mechanical analysis is applied to the flow to identify the upstream fluid structures. These upstream structures show the exact portion of fluid that is going to interact with the swimmer. A mass flow rate is then defined based on the upstream structures, and a metric for propulsive efficiency is established using the mass flow rate and the kinematics of the swimmer. We propose that the unsteady mass flow rate defined by the upstream fluid structures can be used as a metric to measure and objectively compare the efficiency of locomotion in water and air.

Supplementary material available online at http://jeb.biologists.org/cgi/content/full/211/16/2669/DC1

Key words: wake, upstream, fluid dynamics, locomotion.

INTRODUCTION

As a swimming or flying animal moves through its environment, the surrounding water or air is disturbed, resulting in currents of rotating fluid that are left behind in the animal's wake. Over the past few decades, studies of fish swimming (Muller et al., 1997; Drucker and Lauder, 1999; Liao et al., 2003; Wilga and Lauder, 2004; Bartol et al., 2005; Tytell, 2007); bird, bat and insect flight (Spedding et al., 2003; Videler et al., 2004; Warrick et al., 2005; Tian et al., 2006; Hedenstrom et al., 2007; Maxworthy, 1979; Ellington et al., 1996; Dickinson et al., 1999; Wang, 2005) and many other modes of locomotion (Nauwelaerts et al., 2005; Dabiri et al., 2006) have used this wake structure to infer the physical mechanisms governing swimming and flying. However, in each case the focus has been primarily on flow features near the animal appendages or downstream from the animal, based on the assumption that the upstream flow in front of the animal is trivial.

In most studies, the wake vortex structures are identified using velocity, vorticity or streamline plots. Using these methods, no apparent structures are observed in the upstream flow of an animal, especially if the upstream flow is quiescent or has uniform incoming velocity. Recent studies (Haller, 2001; Haller, 2002; Shadden et al., 2005; Shadden et al., 2006) have introduced a new method of fluid dynamics analysis to identify more general types of fluid structures. These coherent structures include vortices but are more generally fluid structures that have distinct dynamics from the surrounding fluid. The new flow analysis method is based on Lagrangian fluid particle trajectories rather than the traditional Eulerian velocity or vorticity plotted at a single time instance. The technique is able to locate vortices in the downstream wake; importantly, it also indicates fluid structures in the upstream flow. For example, coherent fluid structures are observed upstream of a cylinder in cross-flow (Franco et al., 2007) although there is no upstream vorticity (the incoming flow is uniform). Upstream coherent structures are also seen in front of a swimming jellyfish (Shadden et al., 2006; Peng and Dabiri, 2007).

The identification of upstream coherent structures provides researchers with additional information regarding fluid kinematics. Previous research has shown that these upstream structures are indicators of fluid transport (Shadden et al., 2006; Franco et al., 2007). For example, only fluid inside the upstream structures is sampled by a swimming jellyfish; therefore, only prey inside these upstream structures can be captured by the animal.

The correlation between the upstream structures and the energetics of animal locomotion has not been investigated previously. In the present study, we use a computational model to simulate a self-propelled swimmer and identify the upstream fluid structures. A mass flow rate is then defined based on the upstream structures, and a metric for propulsive efficiency is established using the mass flow rate and the kinematics of the swimmer. We propose that, just as the downstream wake has been traditionally correlated to the forces and energetics of locomotion, the heretofore invisible 'upstream wake' also exhibits dynamic significance and variation across animal species that can inform ongoing comparative biological and engineering studies of animal swimming and flying.

MATERIALS AND METHODS

Computational model

A computational model swimmer was created to provide generic locomotion kinematics for this study. The model consists of a flexible flat plate of unit half-length and mass that exhibits time-periodic oscillations of its trailing edge. The shape of the flexible

Fig. 1. Schematic flexible plate model swimmer. s is the curve length and $\Psi(t,s)$ is the tangential angle. LE, leading edge (s=–1); TE, trailing edge (s=1).

Table 1. Kinematics used in the study

Kinematics 1	$\Psi(t,s)=-\tan^{-1}[\varepsilon \sin(\pi s/4)\cos(2\pi ft)]$
Kinematics 2	$\Psi(t,s)=\varepsilon \exp[2(s/L-1/2)\cos(2\pi ft)]$
Kinematics 3	$y(t,s)=\varepsilon \exp[2(s/L-1/2)\cos(2\pi ft)]$

In these mathematical descriptions, variable t is time, f is the stroke frequency, s is the curve length on the plate (from s=–1 at the leading edge to s=1 at the trailing edge), and ε is a parameter indicating the stroke amplitude. Movie 1 in supplementary material illustrates the three kinematics.

plate was prescribed by the tangential angle $\Psi(t,s)$ or by the lateral position $y(t,s)$ in the body frame of reference (Fig. 1). Three different kinematics were used in this study (Table 1).

An inviscid vortex sheet method (Nitsche and Krasny, 1994; Jones, 2003; Shukla and Eldredge, 2007) was used to solve the flow induced by the model swimmer. This method has been validated with experiments in a number of previous studies (Nitsche and Krasny, 1994; Jones, 2003). The solid body was modeled as a bound vortex sheet, and the separated shear layers were modeled as free vortex sheets shed at the trailing edge of the swimmer. In the numerical procedure, the bound vortex sheet attached to the swimmer was discretized and represented as a set of vortex filaments. The position of the bound vortex sheet was known since it coincides with that of the swimmer for all time t. The flow separates at the trailing edge, giving rise to a free shear layer in the flow. A time-stepping procedure was used to release discrete vortex elements of suitable strength from the trailing edge at each step. The unknown bound vortex sheet strength and the edge circulations were solved at each time step by a system of equations satisfying the continuity of the normal velocity across the swimmer, Kelvin's circulation theorem, and the boundedness of the velocity field (Shukla and Eldredge, 2007).

In this inviscid formulation, the hydrodynamic force acting on the swimmer was given by the pressure difference across the flexible plate. The pressure difference across the bound vortex sheet $[p](\mathbf{x},t)$ ('[ ]' indicates the discontinuity across the plate) can be expressed (Jones, 2003) as:

$$[p](\mathbf{x},t) = -\frac{\mathrm{d}\Gamma(\mathbf{x},t)}{\mathrm{d}t} - \sigma(\mathbf{x},t)\big(u(\mathbf{x},t) - \tau(\mathbf{x},t)\big), \qquad (1)$$

where Γ is the circulation, σ is the vortex sheet strength, u is the tangential component of the average velocity at the bound vortex sheet, τ is the tangential component of the velocity of the plate, and $\mathbf{x}$ is the spatial coordinate. The net hydrodynamic force acting on the swimmer is therefore:

$$\mathbf{F}(t) = \int [p](\mathbf{x},t)\mathbf{n}(\mathbf{x},t)\mathrm{d}\mathbf{x}, \qquad (2)$$

where spatial integration over the normal direction $\mathbf{n}(\mathbf{x},t)$ is taken over the plate. The forward motion of the swimmer was computed by integrating the resulting streamwise acceleration that occurs due to this force applied to the swimmer (with unit mass per unit length) by the fluid. Hence, the swimming kinematics and locomotive dynamics in the streamwise direction are fully coupled in the model. For simplicity, the net torque on the swimmer is not fed back into the swimming motion in order to avoid lateral oscillations of the leading edge of the swimmer and the associated vortex shedding.

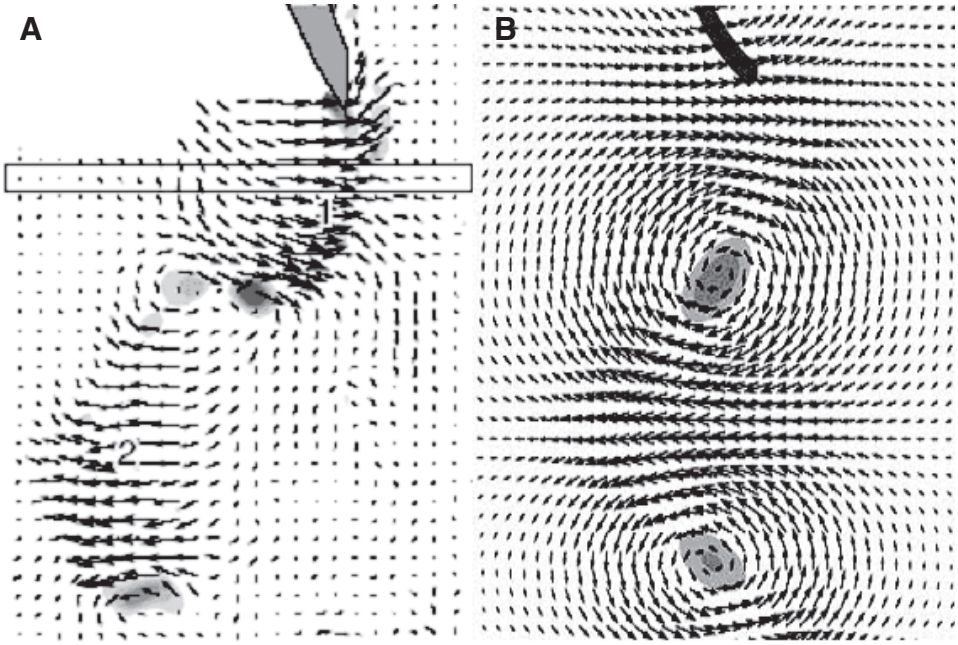

Fig. 2. Flow field from behind an eel. (A) Digital particle image velocimetry (DPIV) measurement (reproduced with permission from Tytell, 2007). (B) Simulation using the vortex sheet method. The key feature of the wake claimed by Tytell and Lauder (Tytell and Lauder, 2004), i.e. the strong lateral jet rather than a downstream jet, is consistent between the simulation and the measurement.

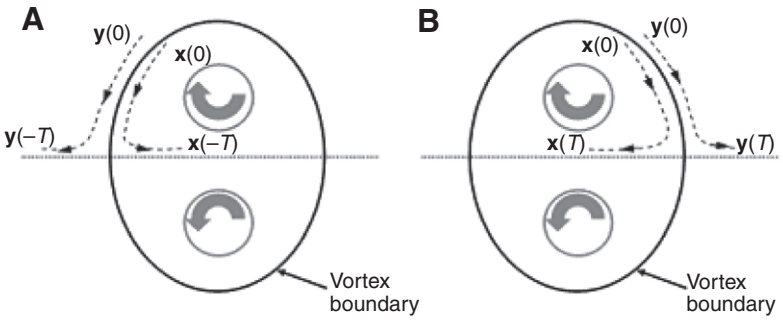

Fig. 3. Schematic of particle separation at the boundary of a vortex ring. (A) Fluid particle pairs straddling the vortex boundary have a larger separation rate in backward time, indicating larger values of backward-time FTLE (finite-time Lyapunov exponent) at the front boundary of the vortex ring. (B) Fluid particle pairs straddling the vortex boundary have a larger separation rate in forward time, indicating larger values of forward-time FTLE at the rear boundary of the vortex ring. **x** and **y** are particle trajectories; T is integration time.

The trailing edge vortex shedding is sufficient to support the conclusions regarding upstream wake dynamics.

To demonstrate that the numerical method used in this study is sufficient to capture the essential features of animal locomotion in fluids, we used the method to compute the flow generated by a specific swimming mode, i.e. anguilliform swimming of an eel (Tytell and Lauder, 2004). The computed flow is consistent with the result of previous digital particle image velocimetry (DPIV) measurements (Fig. 2), with strong lateral jets present in the wake rather than downstream jets; these lateral jets are the key characteristic of eel swimming (Tytell and Lauder, 2004). The self-propelled swimming speed is higher for the model *versus* the real animal [1.9 body lengths s^{-1} (BL s^{-1}) *versus* 1.5 BL s^{-1}], a discrepancy that can be primarily attributed to the lack of skin friction in the vortex sheet model. Despite this effect, the comparable flow kinematics support the notion that the numerical method is appropriate for this proof-of-concept analysis.

FTLE calculation and LCS extraction

To reveal the upstream wake structure, we analyzed the flow using a Lagrangian, or particle-tracking, technique. Specifically, we computed the finite-time Lyapunov exponent (FTLE) field of the flow and identified the Lagrangian Coherent Structure (LCS). The FTLE is defined by:

$$\sigma(\mathbf{x}) = \frac{1}{T}\log\left\|\frac{\delta\mathbf{x}(T)}{\delta\mathbf{x}(0)}\right\|. \quad (3)$$

The FTLE $\sigma(\mathbf{x})$ measures the maximum linearized growth rate of the perturbation $\delta\mathbf{x}$ over the interval T. In other words, it characterizes the amount of fluid particle separation, or stretching, about the trajectory of point **x** over the time interval $[t_0, t_0+T]$. The absolute value $|T|$ is used instead of T in the definition because the FTLE can be computed for $T>0$, indicating fluid particle separation, or for $T<0$, indicating fluid particle attraction (i.e. fluid particle separation in backward time). An illustration is given in Fig. 3, in

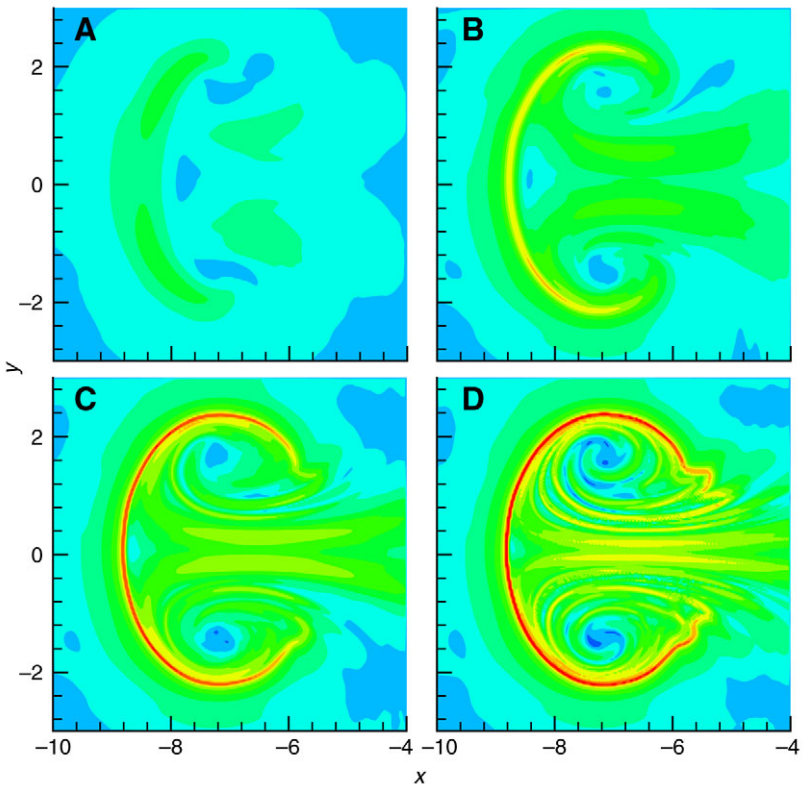

Fig. 4. The effect of integration time on FTLE (finite-time Lyapunov exponent) and LCS (Lagrangian Coherent Structure) calculation for a vortex ring. (A) integration time T=0.4 s; (B) T=1.2 s; (C) T=2.0 s; (D) T=2.8 s. With longer integration time, the FTLE ridges become sharper, i.e. LCS resolve into clearly defined thin lines.

which fluid particle trajectories are used to locate the boundaries of a vortex ring. In Fig. 3A, fluid particle pairs straddling the front vortex boundary diverge faster than any other arbitrary pairs in backward time, indicating a larger value of backward-time FTLE at the front boundary of the vortex ring; in Fig. 3B, fluid particle pairs straddling the rear vortex boundary separate faster than any other arbitrary pairs in forward time, indicating a larger value of forward-time FTLE at the rear boundary of the vortex ring.

A detailed description of FTLE calculation and LCS identification has been given in previous studies (Shadden et al., 2005; Shadden et al., 2006). FTLE calculations for the flow generated by the model swimmer were made using an in-house code (available for download from http://dabiri.caltech.edu/software.html) previously validated in other studies of animal locomotion and fluid–structure interactions (Peng and Dabiri 2007; Peng et al., 2007; Peng and Dabiri, 2008). LCS are defined as ridges of local maxima in the FTLE field. These ridges were extracted visually in the present case, by using an in-house graphical user interface. The uncertainty in this method of LCS extraction is approximately ±5% (Franco et al., 2007). LCS extracted from the forward-time ($T>0$) FTLE fields are repelling LCS, meaning fluid particles separate away from it; LCS extracted from the backward-time ($T<0$) FTLE fields are attracting LCS, meaning fluid particles are attracted to it.

In Eqn 3, The FTLE $\sigma(\mathbf{x})$ is not explicitly written as a function of the integration time T because the length of integration time does not affect the location of the LCS. However, longer integration time can help to more accurately determine the LCS locations by better resolving the ridges of local maxima in the FTLE contour plot. Fig. 4 shows the FTLE for a vortex ring calculated with increasing integration time T. With shorter integration time, the FTLE ridges are thick bands and the precise location of the LCS can be difficult to determine; whereas with longer integration time, the FTLE ridges become sharper, i.e. LCS resolve into clearly defined thin lines. The appropriate length of integration time depends on the particular flow being analyzed, but the 'rule of thumb' regarding the integration time in any LCS analysis is that it should be chosen to be long enough so the LCS is clearly identifiable on the FTLE contour plot. Since the length of integration time only affects the ease and accuracy with which the LCS are determined, it has no effect on foregoing efficiency calculations as long as the integration time is long enough that LCS is clearly defined. The magnitude of the integration time $|T|$ in the present study is four swimming cycles in each case.

RESULTS

Upstream fluid structures

In this section, we show the upstream fluid structures in the flow generated by kinematics 1 in Table 1. A time series of the calculated swimming motion is shown in Fig. 5, as well as the velocity field and vortex wake that it creates (see also Movie 2 in supplementary material). The results are consistent with previous experimental studies of similar modes of locomotion (e.g. Muller et al., 1997). As in previous studies, there is no indication of flow structure in the region upstream of the animal from this perspective.

Fig. 6A shows the backward-time FTLE field. Recall that the backward-time FTLE is computed by observing a reversed time record of the flow; the ridges of high values indicate attracting LCS. As one might expect, attracting LCS coincide with structures revealed in a dye or smoke visualization of a flow, since the fluid labeled by these flow markers will tend to align with the attracting LCS over time. Fig. 6A shows similar behavior for the model swimmer. Comparison with Fig. 5 indicates that the attracting LCS curve is correlated with the configuration of the vortex sheet in the wake.

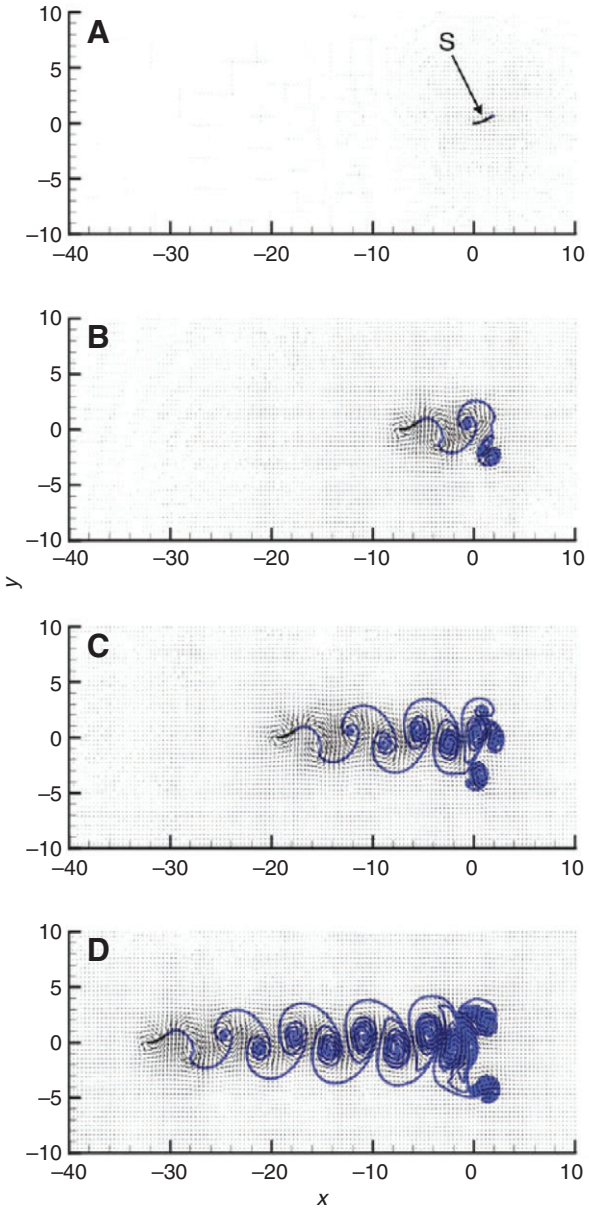

Fig. 5. Locomotion of the model swimmer. The swimmer (S) begins at rest (A) and flaps its flexible body to propel itself forward. The vortex wake generated by the swimming motion (blue curve) and the resulting forward motion of the swimmer are shown after two (B), four (C) and six (D) swimming cycles. See Movie 2 in supplementary material.

By contrast, Fig. 6B plots the forward-time FTLE computed by observing the behavior of the flow as it evolves forward in time. The repelling LCS, located by the ridges' high forward-time FTLE values in the contour plot, are also plotted. What is immediately striking is that this flow structure extends upstream, in front of the swimmer. In fact, the upstream extent of the repelling LCS increases as the amount of information regarding the forward-time behavior of the flow increases, i.e. more of the upstream repelling LCS is revealed as the fluid is tracked over sufficiently long durations to observe its interaction with the swimmer (Shadden et al., 2005). Movie 3 in supplementary material shows the temporal evolution of the FTLE fields and corresponding LCS curves. The morphology of the upstream fluid structures is clearly observable.

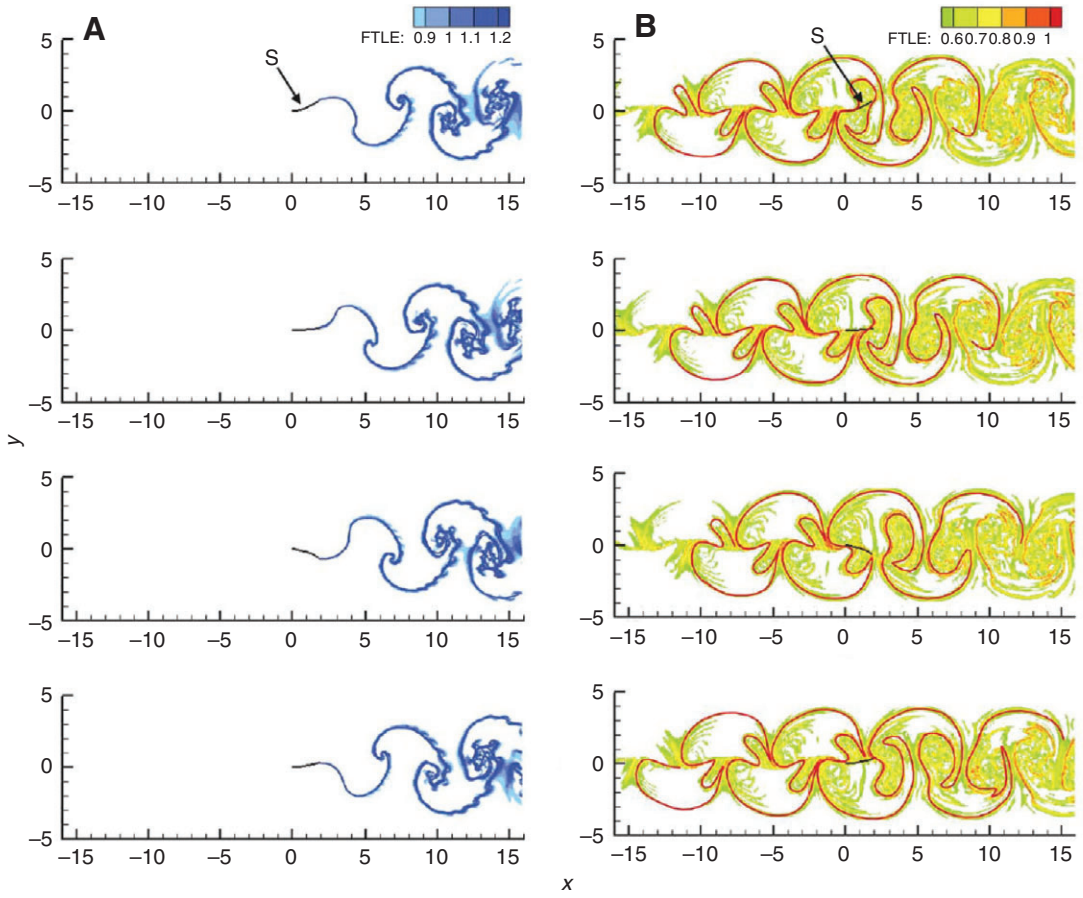

Fig. 6. Finite-time Lyapunov exponent (FTLE) fields of the flow created by the model swimmer (S). Results are presented in a reference frame fixed on the swimmer; the swimmer moves from right to left in a laboratory reference frame (see Fig. 5). Top panel, time t=0; second panel, t=T/5; third panel, t=(2/5)T; bottom panel, t=(4/5)T, where T is the duration of a single swimming cycle. (A) Backward-time FTLE field. The ridge of large FTLE values (solid blue curve) identifies the attracting LCS. (B) Forward-time FTLE field. The ridge of large FTLE values (solid red curve) identifies the repelling LCS. See Movie 3 in supplementary material.

Since fluid is not attracted to the repelling LCS (by definition), the upstream fluid structure, which comprises the repelling LCS, is not readily visualized using passive flow markers (i.e. dye, smoke, etc.) as is the case for the attracting LCS. In addition, since the upstream flow typically possesses a uniform or zero velocity, the repelling LCS propagates without changing its shape until after it reaches the downstream wake (Fig. 6B). By that point, the behavior of the fluid around the swimmer is dominated by the nearby attracting LCS; hence the presence of the repelling LCS is obscured. It is largely for these reasons that the upstream fluid structures have not been observed previously. In the present case, we do not rely on the aggregation of fluid to reveal the repelling LCS. Instead, it is computed based on observed fluid particle separation in the flow. To be sure, we can only visualize the upstream fluid structures by tracking them until the associated repelling LCS has interacted with the swimmer. At this time, fluid particle separation becomes most pronounced, and we can retrospectively identify the upstream fluid structure.

As mentioned previously, a physical significance of the upstream fluid structures is that it indicates the extent of the region around the swimmer that is affected by its locomotion. In fact, in the present paradigm, locomotion is essentially the process whereby a swimming or flying animal transfers fluid from the upstream fluid structure (defined by the repelling LCS) to the downstream wake (defined by the attracting LCS). To demonstrate these concepts, we computationally labeled and tracked the behavior of fluid bounded by adjacent repelling LCS structures in the upstream fluid structure. Fig. 7 indicates that the fluid in the repelling LCS is indeed the source of fluid that comprises the subsequent downstream vortex wake (see also Movie 4 in supplementary material).

Furthermore, fluid in adjacent repelling LCS structures does not mix and is only moderately deformed, thereby maintaining the coherence of the upstream fluid structures. This is in contrast to the behavior of arbitrary fluid parcels placed upstream of the swimmer; these experience large deformations of their shape and exhibit substantial mixing (Fig. 8; see also Movies 5 and 6 in supplementary material). Incidentally, the magnitude of downstream mixing and shape deformation can be predicted by observing the amount of overlap between the interface of the adjacent fluid parcels and the repelling LCS boundaries (Shadden et al., 2007). Despite the fact that the parcels in Fig. 8C cover the same amount of upstream area as each of the repelling LCS labeled in Fig. 7, they do not indicate the full extent of the downstream wake. This illustrates that both the area and the shape of the upstream fluid structures are important for capturing the subsequent downstream wake and locomotive dynamics.

Mass flow rate and a metric for swimming performance

Another goal of the present study is to identify correlations between the geometry of the upstream fluid structures and the propulsive efficiency. One of the most widely used measures of effectiveness of swimming is Froude efficiency, defined as:

$$\eta = \frac{\text{Useful work}}{\text{Total mechanical work}} = \frac{\overline{TU}}{\overline{P}}, \quad (4)$$

where T is thrust, U is swimming speed, P is total mechanical power, and overhead bars indicate time-averaged values over a stroke cycle. However, for undulatory self-propelled bodies, the drag and thrust cannot be separated (Schultz and Webb, 2002). This does not mean that the net hydrodynamic force is zero instantaneously. The force is typically oscillatory, resulting in periodic acceleration and deceleration of the swimmer, as shown in Fig. 9. This leads to 'temporal separation' of thrust and drag and a corresponding, measurable change in momentum flux in the wake (Tytell, 2007). We wish to define an efficiency metric that utilizes the upstream fluid structures to quantify this effect.

To calculate the momentum flux, we first define a mass flow rate based on the upstream fluid structures described above. Since the upstream fluid structures indicated by the LCS show the exact portion of fluid that is going to interact with the swimmer, we can write a time-averaged mass flow rate that is relevant to swimming:

$$\dot{m} = \rho \overline{U} \overline{w}, \quad (5)$$

in which ρ is the fluid density, $\overline{U}$ is the average forward velocity over a stroke cycle, and $\overline{w}$ is the time-average of the width (peak-to-peak in the lateral direction) of the LCS $w(x)$ (see Fig. 7A). The width $w(x)$ is swept out by the upstream wake as it propagates downstream. Given the mass flow rate, the net change in the momentum flux due to periodic acceleration and deceleration of the swimmer can be expressed as $\dot{m}\Delta U$, the product of the mass flow rate and the variation (maximum minus minimum) of swimming velocity of the swimmer over a stroke cycle.

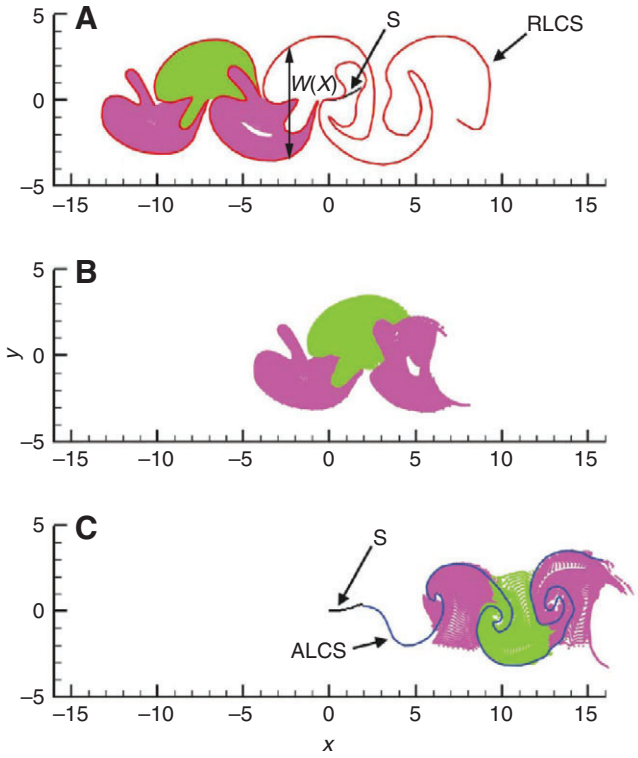

Fig. 7. Temporal evolution of the upstream wake. (A) Time t=0; (B) t=(7/5)T; (C) t=(14/5)T, where T is the duration of a single swimming cycle. See Movie 4 in supplementary material. Fluid particles in each of three adjacent repelling LCS (red curves) are labeled magenta or green in order to track their evolution. After interaction with the swimmer (shown here in a reference frame fixed on the swimmer; the swimmer moves from right to left in a laboratory reference frame; see Fig. 5), the fluid particles in the repelling LCS are shown to comprise the subsequent downstream wake, illustrated by the attracting LCS (blue curves). Fluid particles initially separated by the repelling LCS do not mix and are only moderately deformed. S, swimmer; w(x), the width of the upstream wake; RLCS, repelling LCS; ALCS, attracting LCS.

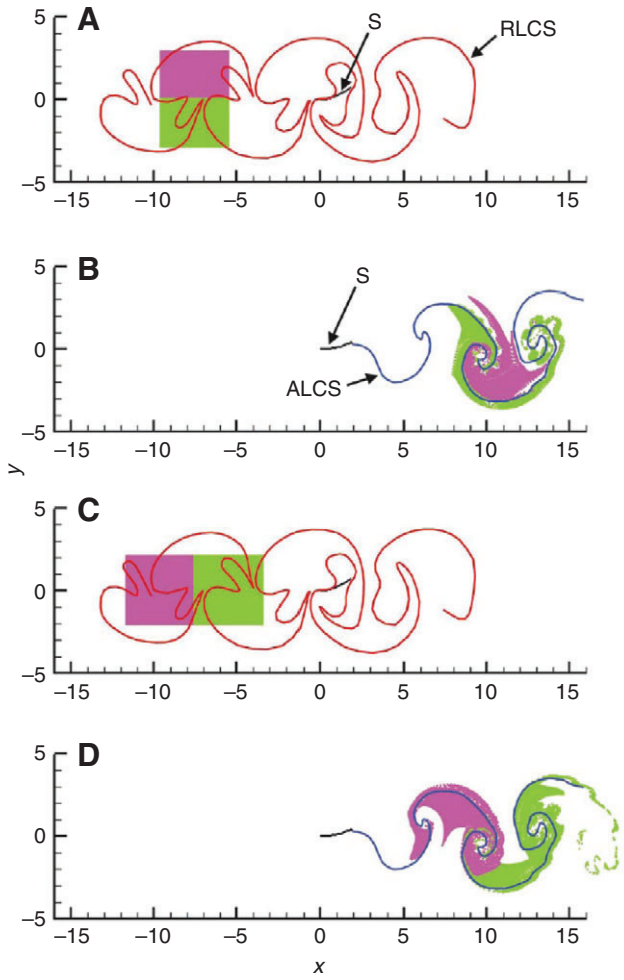

Fig. 8. Temporal evolution of arbitrary upstream fluid parcels. Fluid particles in adjacent regions with a horizontal (A,B) or vertical (C,D) interface are labeled magenta or green in order to track their evolution. The interfaces in both cases do not coincide with the repelling LCS (red curves). After interaction with the swimmer (shown here in a reference frame fixed on the swimmer; the swimmer moves from right to left in a laboratory reference frame; see Fig. 5), the particles in the adjacent parcels exhibit substantial deformation and mixing in the vicinity of the attracting LCS (blue curves). In both cases, the parcels do not indicate the full extent of the downstream wake, in contrast to the repelling LCS parcels in Fig. 7. S, swimmer; RLCS, repelling LCS; ALCS, attracting LCS. (A,C) Time t=0; (B,D) t=(14/5)T, where T is the duration of a single swimming cycle. See Movies 5 and 6 in supplementary material.

Using the momentum flux as a scale for the thrust, a metric for efficiency is introduced as:

$$\eta_{LCS} = \frac{(\dot{m}\Delta U)\bar{U}}{\bar{P}}. \quad (6)$$

Physically, the term in parentheses represents the net momentum flux induced by the animal during locomotion. In the limit of purely steady locomotion (i.e. ΔU=0), there would be no net momentum flux. However, in reality, the forward velocity is only quasi-steady since the reciprocal motion of the appendages causes temporal variations in swimming velocity (Daniel, 1984).

The efficiency of the self-propelled swimmer using each of the kinematics in Table 1 was calculated after the swimmer reached a steady mean velocity (Fig. 9B). The efficiencies are plotted in Fig. 10 against Strouhal number (St=$fA/\bar{U}$, where f is the tail beat frequency, A is the peak-to-peak trailing edge excursion, and $\bar{U}$ is the mean swimming velocity). For each swimming kinematics, the efficiency has a peak, located at St=0.23, 0.18 and 0.27 for kinematics 1, 2 and 3, respectively. This is consistent with previous studies of oscillating foils and flying/swimming animals that indicate optimal propulsive efficiency at Strouhal numbers within the range of 0.2 to 0.4 (Taylor et al., 2003). The efficiency is similar for kinematics 1 and 2 but lower than that of kinematics 3, indicating that kinematics 3 is the best of the three in terms of swimming efficiency.

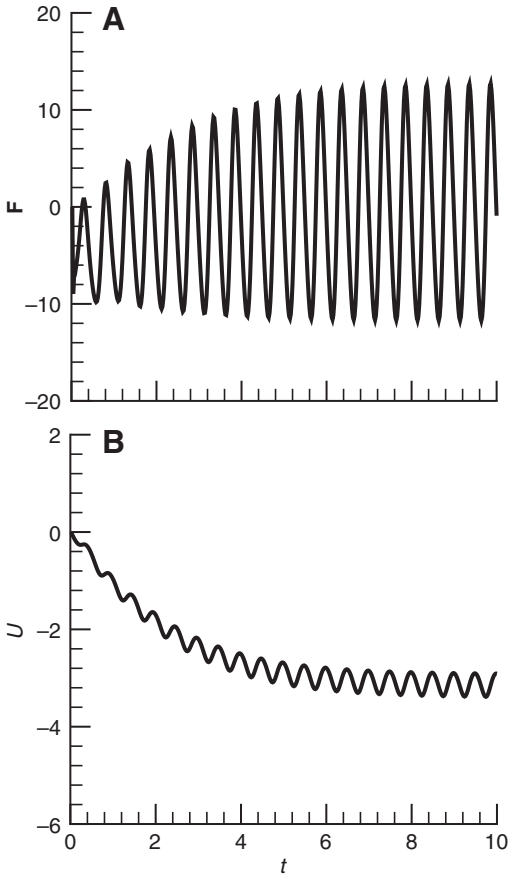

Fig. 9. Total force acting on the swimmer (A) and the velocity of the swimmer (B). The swimmer starts from rest. As it approaches a steady state, i.e. the mean velocity over a stroke cycle approaches a constant, the time average of force approaches zero.

The reason that kinematics 3 has the highest efficiency of the three is that it requires less total power than kinematics 1 and swims faster than kinematics 2.

DISCUSSION

The LCS analysis provides a method to locate the usually 'invisible' upstream fluid structures. The upstream fluid structures can be used to quantify both the magnitude and the geometry of the interaction between animals and their environment. In this study, the cross-stream dimension of the upstream fluid structures is large relative to the size of the animal. The model swimmer suggests that to observe the full extent of the upstream fluid structures in empirical observations of a real animal would require a measurement window many times larger than the animal itself. Notwithstanding this, our recent measurements of free-swimming jellyfish (Shadden et al., 2006; Peng and Dabiri, 2007) indicate the existence of upstream fluid structures in that flow as well, albeit with the possibility that the entire structure was not captured in the measurement. By following fluid particles, it is shown that – similar to the model swimmer – only the fluid inside these upstream structures interacts with the animal (see Movie 7 in supplementary material). Therefore, despite the simplicity of the computational model used here, we hypothesize that the upstream fluid structure is a generic and morphologically diverse feature of locomotion in real fluids.

The upstream fluid structures provide a new focus for fluid dynamic studies of swimming and flying. The upstream structure indicates the portion of fluid that interacts with the animal, thus enabling definition of a mass flow rate induced by locomotion. The new metric for efficiency (η_{LCS}), which is based on change in the momentum flux due to the periodical acceleration of center-of-mass, can be used as a new metric for evaluating swimming performance.

The mass flow rate $\dot{m}$ and the new metric for efficiency η_{LCS} are calculated from the width of the fluid structure w. The width of the fluid structure is larger than the flapping amplitude at the trailing edge, indicating that a larger region of fluid interacts with the swimmer. Fig. 11 also plots an efficiency metric similar to that in Eqn 6 but with the upstream fluid structure width w replaced by the flapping amplitude A. The efficiency based on A does not correlate well with the efficiency based on w. This is because w depends not

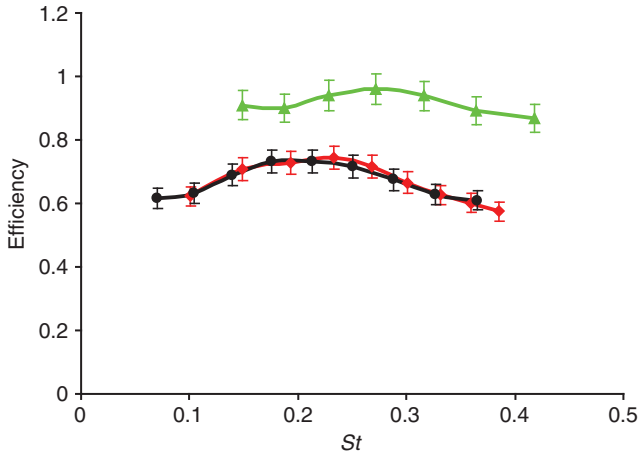

Fig. 10. Efficiency based on mass flow rate (Eqn 6) of the model swimmer *versus* Strouhal number St=$fA/\bar{U}$. Red, kinematics 1; black, kinematics 2; green, kinematics 3. Error bars indicate uncertainty in measurement of upstream wake width.

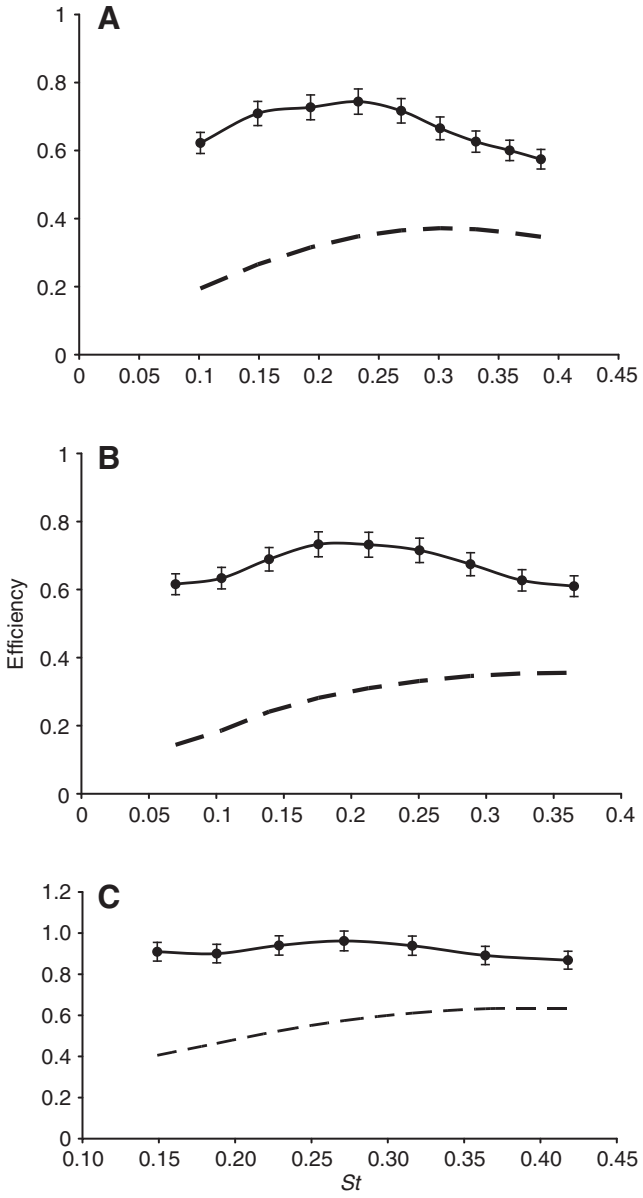

Fig. 11. Comparison of measures for swimming efficiency. Plots A, B and C show kinematics 1, 2 and 3, respectively. Solid lines: efficiency based on the width of the upstream fluid structure; error bars indicate uncertainty in measurement of upstream wake width; broken lines: efficiency calculated by replacing upstream wake width with stroke amplitude of the swimmer (peak-to-peak excursion at trailing edge).

only on A but also on U. To show this, w was calculated for swimming at a constant velocity ($2\,BL\,s^{-1}$) over a range of tail amplitudes and for swimming over a range of velocities with a fixed flapping amplitude (of 1.44 BL). The results are plotted in Fig. 12. The width of the upstream fluid structure scales both with increasing A and with increasing U. Therefore, A provides less information about the locomotion than w, and it cannot take the place of w in the analysis.

Another potentially interesting application of fluid structure shown in this study is to calculate the Strouhal number based on w (as $St=fw/\overline{U}$), which is similar to its classic definition based on the width of the wake for vortex shedding by bluff bodies (e.g. Triantafyllow et al., 1991) rather than the flapping amplitude used in most animal swimming and flying studies. The efficiencies in Fig. 10 are plotted against the modified St in Fig. 13. Because w is larger than A, all three curves shift to the right, with the new peaks located at 1.00, 0.92 and 0.91 for kinematics 1, 2 and 3, respectively. Interestingly, the new peak efficiency for all three kinematics is more tightly constrained using the modified St definition. This result should be investigated further, especially in light of previous studies indicating St tuning for a broad range of swimming and flying animals (Taylor et al., 2003).

A major advantage of using the efficiency metric based on the upstream fluid structures and the mass flow rate is that only flow kinematics (i.e. LCS) and body kinematics (i.e. $\overline{U}$ and ΔU) are required for the measurement. To compare the efficiency of animals or propulsion systems for which the mechanical power input is the same, only the numerator of Eqn 6 is needed. Where needed, the mechanical power $\overline{P}$ may be determined by using existing physiological or mechanical measurement techniques (e.g. Biewener, 2003; Krueger, 2006). Alternatively, the efficiency can be approximated by the ratio:

$$\eta_{LCS} \approx \frac{(\dot{m}\Delta U)\overline{U}}{(\dot{m}\Delta U)\overline{U} + \overline{P}_{wake}}, \quad (7)$$

where P_{wake} is the rate of change of wake kinetic energy, which can be determined from a time record of the velocity field in the wake. This is essentially the rate at which kinetic energy is lost to the wake during locomotion. Importantly, we completely avoid the need to directly measure the locomotive forces, a longstanding challenge in the study of swimming and flying.

The analytical framework developed currently was demonstrated on a model swimmer that does not include the effects of viscous drag. However, the efficiency metric is only affected insofar as the viscous drag contributes to the total mechanical power $\overline{P}$ in the efficiency calculation. The mass flow rate in real flows can still be determined without loss of generality using the methods described here. Where viscous losses are neglected, the proposed efficiency

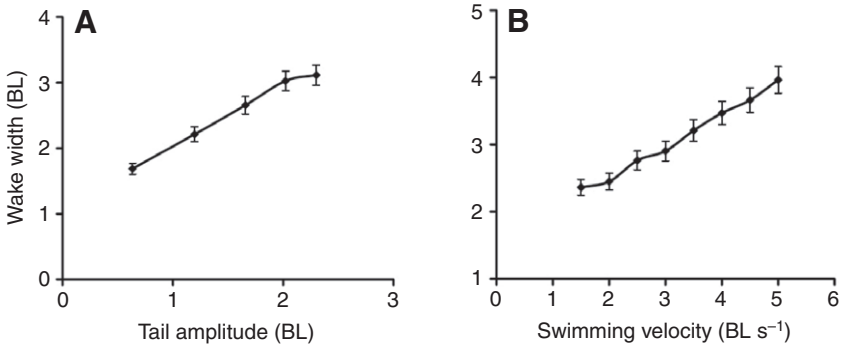

Fig. 12. The width of the wake. (A) Wake width of a swimmer swimming at a constant velocity ($2\,BL\,s^{-1}$) with different tail amplitudes. (B) Wake width of a swimmer swimming at different velocities with the same body kinematics (flapping amplitudes of 1.44 BL).

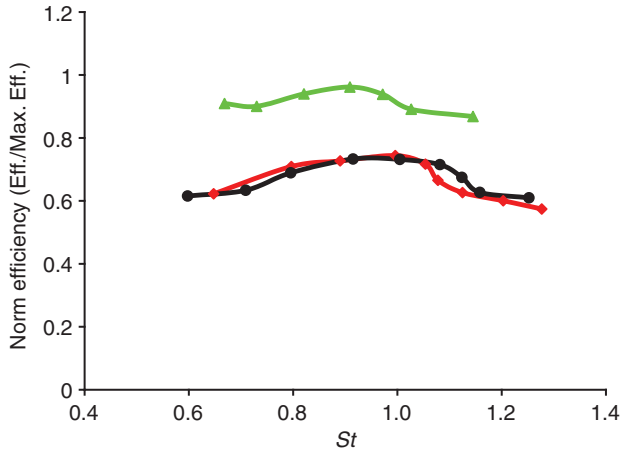

Fig. 13. Efficiency of the swimmer *versus* modified Strouhal number $St=fw/\bar{U}$. Red, kinematics 1; black, kinematics 2; green, kinematics 3.

metric will overestimate the true performance (i.e. since the denominator of the efficiency will be underestimated). In theory, the proposed measure is most accurate when the power loss due to friction, P_{fric}, is small relative to the total mechanical power, $\bar{P}=P_{\text{prop}}+P_{\text{wake}}+P_{\text{fric}}$, where P_{prop} and P_{wake} are useful power for propulsion and wake power, respectively. Equivalently, we require that the Reynolds number, Re, is $\gg \rho a U^3/(P_{\text{prop}}+P_{\text{wake}})$, where a is the wetted surface area of the swimmer. The Reynolds number relationship reflects the relative importance of inertial effects (embodied in the $\rho a U^3$ term) and viscous effects (embodied in P_{fric}).

When applying the proposed methods to particle image velocimetry (PIV) measurements, the field of view should be large enough to cover some distance upstream of the animal. For animals with periodic stroke patterns, the LCS is also periodic with the same frequency (or an integer multiple thereof). Hence, the distance upstream of the animal should be equal to or larger than the distance the animal can swim during a stroke cycle, i.e. swimming velocity multiplied by stroke period. The proposed method is also robust to noise in PIV measurements. It has been demonstrated that large velocity errors still preserve reliable predictions on Lagrangian coherent structures, as long as the errors remain small in a special time-weighted norm (Haller, 2002).

Although the analytical framework was demonstrated in a two-dimensional flow, the analysis can be extended to three-dimensional flows, in which the LCS are surfaces rather than curves. Although volumetric flow measurements are ideal for this purpose, two-dimensional PIV data can also be utilized by collecting measurements on multiple parallel planes. The mass flux per unit depth in each plane can then be summed to determine the total mass flux. A potential advantage of the present methods is that, given the fact that Eulerian PIV is more difficult than Lagrangian particle tracking velocimetry in three-dimensional flows, the present analysis would be especially well suited to three-dimensional experiments since LCS can be directly calculated from particle trajectories.

In summary, the upstream fluid structures visualized by the LCS analysis provide new information regarding the interaction between swimming/flying animals and the fluid environment. These animal–fluid interactions have broad consequences for predation, reproduction and other behavioral functions. As previous measurements of animal swimming and flying are re-examined and new observations are made using the methods described here, the upstream fluid structures can become as useful as the downstream wake has traditionally been for comparative biological and engineering studies of animal locomotion.

We thank Dr Robert Krasny, Dr Jeff Eldredge and Dr Ratnesh Shukla for discussions of the vortex sheet method. We also thank Dr George Lauder for discussions of eel swimming. We gratefully acknowledge financial support from the National Science Foundation programs in Biological Oceanography (OCE-0623475, OCE-0727825) and Energy for Sustainability (CBET-0725164) and an ONR Young Investigator Program award (to J.O.D.).

REFERENCES

Bartol, I. K., Gharib, M., Webb, P. W., Weihs, D. and Gordon, M. S. (2005). Body-induced vortical flows: a common mechanism for self-corrective trimming control in boxfishes. *J. Exp. Biol.* **208**, 327-344.
Biewener, A. (2003). *Animal Locomotion*. Oxford: Oxford University Press.
Dabiri, J. O., Colin, S. P. and Costello, J. H. (2006). Fast-swimming hydromedusae exploit velar kinematics to form an optimal vortex wake. *J. Exp. Biol.* **209**, 2025-2033.
Daniel, T. L. (1984). Unsteady aspects of aquatic locomotion. *Am. Zool.* **24**, 121-134.
Dickinson, M. H., Lehmann, F. O. and Sane, S. P. (1999). Wing rotation and the aerodynamic basis of insect flight. *Science* **284**, 1954-1960.
Drucker, E. G. and Lauder, G. V. (1999). Locomotor forces on a swimming fish: three-dimensional vortex wake dynamics quantified using digital particle image velocimetry. *J. Exp. Biol.* **202**, 2393-2412.
Ellington, C. P., van den Berg, C., Willmott, A. P. and Thomas, A. L. R. (1996). Leading edge vortices in insect flight. *Nature* **384**, 626-630.
Franco, E., Pekarek, D. N., Peng, J. and Dabiri, J. O. (2007). Geometry of unsteady fluid transport during fluid-structure interactions. *J. Fluid Mech.* **589**, 125-145.
Haller, G. (2001). Distinguished material surfaces and coherent structures in 3D fluid flows. *Physica D* **149**, 248-277.
Haller, G. (2002). Lagrangian coherent structures from approximate velocity data. *Phys. Fluids* **14**, 1851-1861.
Hedenstrom, A. et al. (2007). Bat flight generates complex aerodynamic tracks. *Science* **316**, 894-897.
Jones, M. A. (2003). The separated flow of an inviscid fluid around a moving flat plate. *J. Fluid Mech.* **496**, 405-441.
Krueger, P. S. (2006). Measurement of propulsive power and evaluation of propulsive performance from the wake of a self-propelled vehicle. *Bioinspir. Biomim.* **1**, 49-56.
Liao, J. C., Beal, D. N., Lauder, G. V. and Triantafyllou, M. S. (2003). Fish exploiting vortices decrease muscle activity. *Science* **302**, 1566-1569.
Maxworthy, T. (1979). Experiments on the Weis-Fogh mechanism of lift generation by insects in hovering flight. Part 1. Dynamics of the 'fling'. *J. Fluid Mech.* **93**, 47-63.
Muller, U. K., Van den Heuvel, B. L. E., Stamhuis, E. J. and Videler, J. J. (1997). Fish foot prints: Morphology and energetics of the wake behind a continuously swimming mullet (*Chelon labrosus* Risso). *J. Exp. Biol.* **200**, 2893-2906.
Nauwelaerts, S., Stamhuis, E. J. and Aerts, P. (2005). Propulsive force calculations in swimming frogs I. A momentum-impulse approach. *J. Exp. Biol.* **208**, 1435-1443.
Nitsche, M. and Krasny, R. (1994). A numerical study of vortex ring formation at the edge of a circular tube. *J. Fluid Mech.* **276**, 139-161.
Peng, J. and Dabiri, J. O. (2007). A potential-flow, deformable-body model for fluid–structure interactions with compact vorticity, application to animal swimming measurements. *Exp. Fluids* **43**, 655-664.
Peng, J. and Dabiri, J. O. (2008). An overview of a Lagrangian method for analysis of animal wake dynamics. *J. Exp. Biol.* **211**, 280-287.
Peng, J., Dabiri, J. O., Madden, P. G. and Lauder, G. V. (2007). Non-invasive measurement of instantaneous forces during aquatic locomotion: a case study of the bluegill sunfish pectoral fin. *J. Exp. Biol.* **210**, 685-698.
Schultz, W. W. and Webb, P. W. (2002). Power requirements of swimming: Do new methods resolve old questions? *Integr. Comp. Biol.* **42**, 1018-1025.
Shadden, S. C., Lekien, F. and Marsden, J. E. (2005). Definition and properties of Lagrangian coherent structures from finite-time Lyapunov exponents in two-dimensional aperiodic flows. *Physica D* **212**, 271-304.
Shadden, S. C., Dabiri, J. O. and Marsden, J. E. (2006). Lagrangian analysis of fluid transport in empirical vortex ring flows. *Phys. Fluids* **18**, 047105.
Shadden, S. C., Katija, K., Rosenfeld, M., Marsden, J. E. and Dabiri, J. O. (2007). Transport and stirring induced by vortex formation. *J. Fluid Mech.* **593**, 315-331.
Shukla, R. K. and Eldredge, J. D. (2007). An inviscid model for vortex shedding from a deforming body. *Theor. Comp. Fluid Dyn.* **21**, 343-368.
Spedding, G. R., Rosen, M. and Hedenstrom, A. (2003). A family of vortex wakes generated by a thrush nightingale in free flight in a wind tunnel over its entire natural range of flight speeds. *J. Exp. Biol.* **206**, 2313-2344.
Taylor, G. K., Nudds, R. L. and Thomas, A. L. (2003). Flying and swimming animals cruise at a Strouhal number tuned for high power efficiency**.** *Nature* **425**, 707-711.
Tian, X. et al. (2006). Direct measurements of the kinematics and dynamics of bat flight Bioinsp. *Bioinspir. Biomim.* **1**, S10-S18.
Triantafyllou, M. S., Triantafyllou, G. S. and Gopalkrishnan, R. (1991). Wake mechanics for thrust generation in oscillating foils. *Phys. Fluids A* **3**, 2835-2837.
Tytell, E. D. (2007). Do trout swim better than eels? Challenges for estimating performance based on the wake of self-propelled bodies. *Exp. Fluids* **43**, 701-712.
Tytell, E. D. and Lauder, G. V. (2004). The hydrodynamics of eel swimming. I. Wake structure. *J. Exp. Biol.* **207**, 1825-1841.
Videler, J. J., Stamhuis, E. J. and Povel, G. D. E. (2004). Leading-edge vortex lifts swifts. *Science* **306**, 1960-1962.
Wang, Z. J. (2005). Dissecting insect flight. *Annu. Rev. Fluid Mech.* **37**, 183-210.
Warrick, D. R., Tobalske, B. W. and Powers, D. R. (2005). Aerodynamics of the hovering hummingbird. *Nature* **435**, 1094-1097.
Wilga, C. D. and Lauder, G. V. (2004). Hydrodynamic function of the shark's tail. *Nature* **430**, 850.